Saturn's emitted power

Liming Li,[1,2] Barney J. Conrath,[2] Peter J. Gierasch,[2] Richard K. Achterberg,[3]
Conor A. Nixon,[3] Amy A. Simon-Miller,[4] F. Michael Flasar,[4] Don Banfield,[2]
Kevin H. Baines,[5] Robert A. West,[5] Andrew P. Ingersoll,[6] Ashwin R. Vasavada,[5]
Anthony D. Del Genio,[7] Carolyn C. Porco,[8] Andrei A. Mamoutkine,[9] Marcia E. Segura,[10]
Gordon L. Bjoraker,[4] Glenn S. Orton,[5] Leigh N. Fletcher,[11] Patrick G. J. Irwin,[11]
and Peter L. Read[11]

[1] Long-term (2004–2009) on-orbit observations by Cassini Composite Infrared Spectrometer are analyzed to precisely measure Saturn's emitted power and its meridional distribution. Our evaluations suggest that the average global emitted power is 4.952 ± 0.035 W m^{-2} during the period of 2004–2009. The corresponding effective temperature is 96.67 ± 0.17 K. The emitted power is 16.6% higher in the Southern Hemisphere than in the Northern Hemisphere. From 2005 to 2009, the global mean emitted power and effective temperature decreased by ~2% and ~0.5%, respectively. Our study further reveals the interannual variability of emitted power and effective temperature between the epoch of Voyager (~1 Saturn year ago) and the current epoch of Cassini, suggesting changes in the cloud opacity from year to year on Saturn. The seasonal and interannual variability of emitted power implies that the energy balance and internal heat are also varying.

Citation: Li, L., et al. (2010), Saturn's emitted power, *J. Geophys. Res.*, *115*, E11002, doi:10.1029/2010JE003631.

1. Introduction

[2] The relationship between emitted thermal energy and absorbed solar energy for a planet is generally called the energy balance [*Conrath et al.*, 1989]. An internal heat source is inferred for the planet if the emitted thermal energy exceeds the absorbed solar energy. The internal heat and its meridional distribution play a critical role in analytical and numerical models of the large-scale atmospheric circulations of the giant planets [*Busse*, 1976, 1983; *Christensen*, 2001; *Li et al.*, 2006; *Heimpel and Aurnou*, 2007; *Aurnou et al.*, 2007; *Chan and Mayr*, 2008; *Showman*, 2008; *Schneider and Liu*, 2008]. The energy balance and associated internal heat also pro-

vide clues to the internal structure and evolution of giant planets [*Smoluchowski*, 1976; *Salpeter*, 1973; *Flasar*, 1973; *Stevenson and Salpeter*, 1976].

[3] The calculation of the energy balance depends on precise measurements of the emitted thermal energy and the absorbed solar energy. We here explore the energy balance of Saturn through observations from the Cassini spacecraft. In this paper, we evaluate the emitted thermal radiance of Saturn based on measurements made by the Cassini composite infrared spectrometer (CIRS). In subsequent papers, we will report on the absorbed solar radiance of the planet as observed by Cassini imaging science subsystem (ISS) and visual and infrared mapping spectrometer (VIMS).

[4] The emitted thermal energy of Saturn has been addressed in previous studies based on observations conducted using ground-based telescopes [*Nolt et al.*, 1977], airborne telescopes [*Aumann et al.*, 1969; *Wright*, 1976; *Ward*, 1977; *Erickson et al.*, 1978; *Courtin et al.*, 1979; *Gautier and Courtn*, 1979; *Hass et al.*, 1982; *Melnick et al.*, 1983], and infrared instruments aboard Pioneer and Voyager [*Ingersoll et al.*, 1980; *Orton and Ingersoll*, 1980; *Hanel et al.*, 1983; *Ingersoll*, 1990]. Comprehensive reviews of these previous studies are given by *Hanel et al.* [1983] and *Conrath et al.* [1989]. The precise measurement of the total thermal energy of Saturn must take into account the spectrally integrated planetary thermal flux over all emission angles. Observations at different latitudes of Saturn are also required if we want to resolve the meridional distribution of emitted power and energy balance. All of these previous measurements have some limitations in the coverage of wavelength,

[1]Department of Earth and Atmospheric Sciences, University of Houston, Houston, Texas, USA.
[2]Department of Astronomy, Cornell University, Ithaca, New York, USA.
[3]Department of Astronomy, University of Maryland, College Park, Maryland, USA.
[4]NASA Goddard Space Flight Center, Greenbelt, Maryland, USA.
[5]Jet Propulsion Laboratory, California Institute of Technology, Pasadena, California, USA.
[6]Division of Geological and Planetary Sciences, California Institute of Technology, Pasadena, California, USA.
[7]NASA Goddard Institute for Space Studies, New York, New York, USA.
[8]CICLOPS/Space Science Institute, Boulder, Colorado, USA.
[9]Science Systems and Applications Inc., Lanham, Maryland, USA.
[10]QSS Group, Inc., Lanham, Maryland, USA.
[11]Atmospheric, Oceanic and Planetary Physics, University of Oxford, Oxford, UK.

Table 1. Parameters of the Infrared Instruments of Pioneer, Voyager, and Cassini[a]

	Pioneer 11	Voyager 1/2	Cassini
Instruments	Radiometer	Interferometer/Radiometer	Interferometer
Spectral Range (cm^{-1})	180–330 and 400–715	180–2500/5000–30,000	10–1400
Spectral Range (μm)	30–56 and 14–25	4–55/0.33–2	7–1000
Spectral Resolution (cm^{-1})	–	4.3/–	0.5–15.5
Field of View (°)	0.3 × 1.0 (longitude × latitude)	4.28 (circular)	0.22(FP1) (circular)

[a]For more characteristics, please refer to *Bender et al.* [1974], *Hanel et al.* [1980], and *Flasar et al.* [2004] for Pioneer, Voyager, and Cassini, respectively.

emission angle, and latitude. In contrast, the on-orbit observations of Saturn by Cassini/CIRS are nearly complete in the coverage of these variables, thus providing the means for a precise measurement of Saturn's emitted power and its meridional distribution. In addition, the long-term observations of Saturn by Cassini provide for the first time an opportunity to examine the seasonal variability in the emitted power of the giant planet. Finally, the comparison of emitted power and associated energy balance among the epochs of Pioneer, Voyager, and Cassini provides new insight into the interannual variability of Saturn.

2. Methodology

[5] The emitted energy per unit time over a unit area is called emitted power. The emitted power (P_{emit}), in the format of spectral flux I_ν, is defined as [*Chandrasekhar*, 1950; *Goody and Yung*, 1989; *Hanel et al.*, 2003]

$$
\begin{aligned}
P_{\text{emit}} &= \int_{\nu_1}^{\nu_2} \int_\omega I_\nu(\delta, \phi) \cos \delta \; d\omega \; d\nu \\
&= \int_{\nu_1}^{\nu_2} \int_0^{2\pi} \int_0^{\pi/2} I_\nu(\delta, \phi) \cos \delta \; \sin \delta \; d\delta \; d\phi \; d\nu,
\end{aligned} \tag{1}
$$

where ν is the wave number, δ is the emission angle, ϕ is the azimuth angle, and ω is the solid angle. In a real atmosphere, it is generally valid to assume that for emitted power radiation the spectral flux $I_\nu(\delta, \phi)$ depends only on the emission angle δ and not on the azimuth angle ϕ [*Hanel et al.*, 1983]. Therefore, the emitted power P_{emit} can be simplified into the form

$$
\begin{aligned}
P_{\text{emit}} &= 2\pi \int_{\nu_1}^{\nu_2} \int_0^{\pi/2} I_\nu(\delta) \cos \delta \; \sin \delta \; d\delta \; d\nu \\
&\approx 2\pi \sum_{\delta_j} \sum_{\nu_i} I_{\nu_i}(\delta_j) \cos \delta_j \; \sin \delta_j \; \Delta\delta\Delta\nu \\
&= 2\pi \sum_{\delta_j} \left(\sum_{\nu_i} I_{\nu_i}(\delta_j) \Delta\nu \right) \cos \delta_j \; \sin \delta_j \; \Delta\delta \\
&= 2\pi \sum_{\delta_j} I(\delta_j) \cos \delta_j \; \sin \delta_j \; \Delta\delta,
\end{aligned} \tag{2}
$$

where $I(\delta_j) = \sum_{\nu_i} I_{\nu_i}(\delta_j)\Delta\nu$. We approximate the integration with a sum in equation (2) because we have measurements of $I_{\nu_i}(\delta_j)$ at discrete wavelength and emission angle instead of a continuous function of $I_\nu(\delta)$. The multiple measurements (if any) of emitted power at latitude ϕ are averaged into the zonal mean emitted power $P_{\text{emit}}(\phi)$. Then the corresponding zonal average effective temperature $T_{\text{eff}}(\phi)$, which is defined as the temperature of a blackbody emitting the same total power, can be evaluated from the zonal mean emitted power

$P_{\text{emit}}(\phi)$. We use planetographic latitude ϕ in this paper, except where specifically mentioned.

[6] After calculating the emitted power $P_{\text{emit}}(\phi)$ at all latitudes, we can evaluate the average global emitted power and effective temperature of Saturn. The average emitted power $\overline{P}_{\text{emit}}$ over the globe of Saturn, which is approximated with an oblate spheroid, can be expressed as [*Ingersoll et al.*, 1975]

$$
\overline{P}_{\text{emit}} = \frac{1}{2(1 - 2\varepsilon/3)} \int_{-\pi/2}^{\pi/2} \left(1 - 2\varepsilon \sin^2 \phi'\right) P_{\text{emit}}(\phi') \cos \phi' \; d\phi', \tag{3}
$$

where ε is the oblateness of Saturn and ϕ' is the planetocentric latitude. We convert the planetographic latitude ϕ to the planetocentric latitude ϕ' by the relationship $\tan\phi' = (1 - \varepsilon)^2 \tan\phi$ before using equation (3). Then we have the average global effective temperature $\overline{T}_{\text{eff}}$ as

$$
\overline{T}_{\text{eff}} = \left(\overline{P}_{\text{emit}}/\sigma\right)^{(1/4)}, \tag{4}
$$

where σ is the Stefan-Boltzmann constant.

[7] On the basis of this analytical framework, we use all CIRS radiances of Saturn's atmosphere during the period of 2004–2009 to calculate the emitted power and effective temperature of Saturn. Note that, when using CIRS data, we avoid contaminated spectra recorded when CIRS was pointed toward Saturn's rings.

3. CIRS Observations and Data Processing

3.1. CIRS Introduction

[8] The emitted thermal radiance over a wide range of wave numbers and emission angles ($I_{\nu_i}(\delta_j)$) is critical for the accurate evaluation of the emitted power of Saturn. Onboard Cassini, the composite infrared spectrometer (CIRS), a Fourier-transform spectrometer described elsewhere [*Flasar et al.*, 2004], provides such information. Compared to Pioneer's infrared radiometer (IRR) and Voyager's Infrared Interferometer Spectrometer (IRIS), Cassini's CIRS has extended far-infrared coverage and better spectral resolution (Table 1). As an orbiting platform observing Saturn, Cassini has an inherent advantage over its predecessors, the Pioneer spacecraft and the twin Voyager spacecraft, which made only flyby observations of Saturn. The on-orbit global observations of Saturn by Cassini cover almost all viewing geometries, so that measurements of thermal radiance from pole to pole at nearly all emission angles are obtained, enabling computation of the emitted power of Saturn and its meridional distribution. In addition, Cassini has already observed Saturn over a 6 Earth year period (October 2004 to March 2010), including an equinox geometry (August 2009), thus
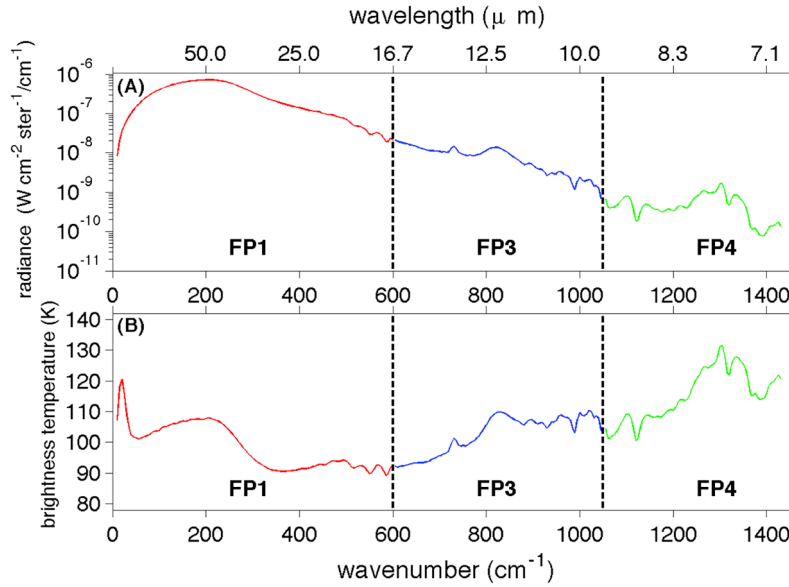
Figure 1. Combined spectral flux I_ν from the three spectra obtained by FP1, FP3, and FP4. The combined spectrum has wave number ranges 5–600 cm^{-1}, 600–1050 cm^{-1}, and 1055–1430 cm^{-1} for FP1, FP3, and FP4, respectively. The zonal-mean spectrum, which was recorded at a spectral resolution of 15 cm^{-1} in 1 September 2007, has latitude ~10°S and emission angle ~10°. (a) CIRS radiance. (b) Corresponding brightness temperature.

providing relevant measurements for examination of the seasonal variability of emitted power and energy balance of the giant planet. The Saturn flyby observations conducted by Pioneer 11 (September 1979) and Voyager 1/2 (November 1980 and August 1981) are roughly 1 Saturn year before the current epoch of Cassini, so a comparison of emitted power and energy balance between this study and earlier analyses of observations by Pioneer 11 and Voyager 1/2 sheds light on the interannual variability of Saturn.

3.2.   Wavenumber Selection

[9] There are three focal planes (FP1, FP3, and FP4) in the CIRS instrument, which have an effective wave number range from 10 to 1430 cm^{-1} [*Kunde et al.*, 1996; *Nixon et al.*, 2009, Appendix A]. The CIRS spectral coverage extends to the far-infrared (wave number < 200 cm^{-1}, i.e., wavelength > 50 μm), a spectral range not covered by the Pioneer IRR and Voyager IRIS. The wave number ranges are 10–695 cm^{-1} (~14–1000 μm), 570–1125 cm^{-1} (~9–18 μm), and 1025–1430 cm^{-1} (~7–10 μm) for focal planes FP1, FP3, and FP4, respectively. Sensitivity decreases toward the ends of each range; therefore, noise increases in the wave number overlap regions of the three focal planes, which will be avoided in our evaluation of the emitted power of Saturn. Our analyses show that choosing wave number ranges 10–600 cm^{-1} (~17–1000 μm) for FP1, 600–1050 cm^{-1} (~10–17 μm) for FP3, and 1050–1430 cm^{-1} (~7–10 μm) for FP4 provide the best instrument performance. A combined CIRS spectral flux I_ν from FP1, FP3, and FP4 at a spectral resolution of 15 cm^{-1} is presented in Figure 1. CIRS has an adjustable spectral resolution varying from 0.5 to 15 cm^{-1}; we mainly utilize observations made at resolutions of 3 and 15 cm^{-1} as they have the best spatial coverage.

[10] Figure 1 shows that the radiance observed by FP1 is larger than the radiance observed by FP3 and FP4 by 1 and 2 orders of magnitude, respectively. Therefore, the focal plane FP1 records most of the emitted power of Saturn. The spectra recorded by FP3 and FP4 include some emission/absorption bands in the troposphere and stratosphere, which are displayed more clearly in Figure 1b. The radiance from these emission/absorption bands also contributes to the emitted power of Saturn, and so we include the FP3 and FP4 spectral ranges in our analysis to improve the accuracy of the results.

3.3.   Data Processing

[11] Almost all CIRS radiances of Saturn's atmosphere that avoid the ring-contaminated data are included in this study; in total, several million CIRS spectra were taken between October 2004 and December 2009. A very small fraction ($<0.01\%$) of these recorded CIRS radiances have values much larger/smaller than the reasonable range of radiance from Saturn and are thought to be bad records: these are removed from the selection. We organize these spectra into 4-D (longitude × latitude × emission angle × wave number) matrices for different Earth years and different spectral resolutions. The resolutions are 30°, 1°, and 1° in longitude, latitude, and emission angle, respectively. The spectral resolution of the organized matrices varies. The 4-D matrices are then averaged along the zonal direction into the 3-D (latitude × emission angle × wave number) matrices. Finally, these matrices are integrated over wave number ranges 10–600, 600–1050, and 1050–1430 cm^{-1} for FP1, FP3, and FP4, respectively. The final data products are 2-D (latitude × emission angle) matrices for different times and different spectral resolutions.
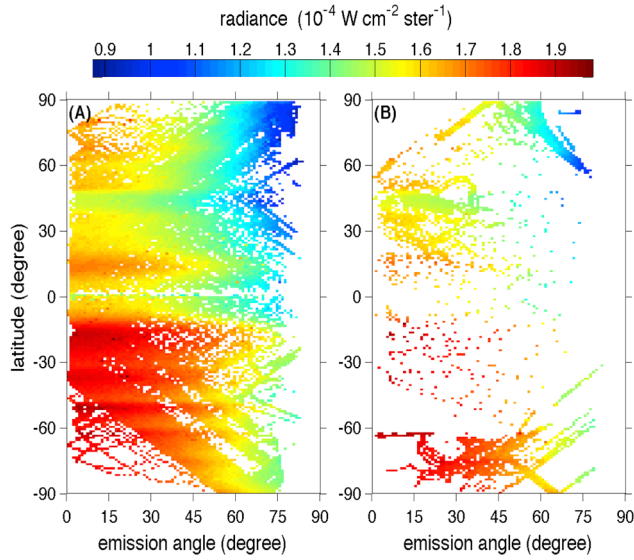
Figure 2. Coverage of wave number-integrated CIRS radiance in the plane of latitude and emission angle with different spectral resolutions. The CIRS radiance shown here was recorded by the focal plane FP1 in 2008. (a) Radiance at a spectral resolution of 15 cm^{-1}. (b) Radiance at a spectral resolution of 3 cm^{-1}.

[12] Figure 2 displays an example of the final matrices in the plane of latitude and emission angle, which were recorded through the whole 2008. Figure 2a is the CIRS radiance with a spectral resolution of 15 cm^{-1}, which covers roughly from 0° to 75° along the direction of emission angle for all latitudes except for the polar regions and the narrow latitude band around the equator. Figure 2b is the radiance with a spectral resolution of 3 cm^{-1}, which covers much less of the parameter space in latitude and emission angle. Only the coverage of radiance recorded by FP1 is shown in Figure 2. The coverage of radiance by FP3 and FP4, which is roughly the same as that of FP1, is not shown here. Compared with the radiance coverage at spectral resolutions of 15 and 3 cm^{-1}, that of other spectral resolutions is negligible, so we focus on those two resolutions in this work. Figure 2 also shows that the overlap areas between Figures 2a and 2b, which are observed by both spectral resolutions (15 and 3 cm^{-1}), have the roughly similar radiances. Therefore, we merge matrices at these two resolutions into a single 2-D matrix.

[13] The matrices at different Earth years are averaged together to represent the average radiance of Saturn during the period of 2004–2009. Figure 3 displays the temporal mean radiance in the plane of latitude and emission angle, recorded by each of the three focal planes. First, we note that some banded structures of radiance along the direction of latitude are displayed in the observations. The time period of 2004–2009 covers the winter season for the Northern Hemisphere (NH), so the radiance in the Southern Hemisphere (SH) is generally larger than the radiance in the NH. Figure 3a also shows that the radiance decreases with increasing emission angle. The radiance in the wave number range of FP1 (5–600 cm^{-1}) mainly comes from the troposphere and probes higher altitudes at high emission angles than at low emission angles, where atmospheric temperature decreases in Saturn's

troposphere. Therefore, the radiance recorded by FP1 at high emission angles, which mainly comes from the relatively high and hence cold troposphere, is smaller than the recorded radiance at low emission angles, which originates lower down where temperatures are warmer. In contrast, the radiance in wave number range of FP3 and FP4 (605–1430 cm^{-1}) increases with emission angle at most latitudes. There are many stratospheric emission bands located in the wave number range of FP3 and FP4. Since temperature increases with altitude in the stratosphere of Saturn, the radiance recorded by FP3 and FP4 at high emission angles, coming from the relatively high and hence hot atmosphere, is larger than the radiance at low emission angles from the colder lower stratosphere. In summary, the vertical thermal structures of Saturn's atmosphere can explain the variance of radiance with emission angle for each focal plane due to the atmospheric levels sounded. In addition, Figures 3b and 3c show that the radiance of the polar region in the SH is higher at high emission angles than at low emission angles, which are due to the hot temperatures within the south polar region in the stratosphere [*Fletcher et al.*, 2010]. It should be mentioned that Figure 3c (FP4) shows some diagonal lines, which are related to the observational footprints. These diagonal lines are probably due to the temporal variance of radiance and possible calibration artifacts. The radiance recorded by FP4 is less than 0.1% of the total emitted power, so the biases related to these diagonal lines in FP4 do not affect our evaluations of emitted power significantly.

3.4. Filling of Observational Gaps

[14] The variance of radiance with emission angle, which is shown in Figure 3, can be qualitatively explained by the vertical thermal structures of the troposphere and stratosphere, as discussed in section 3.3. However, it is difficult to quantitatively predict the variance of radiance with varying emission angle because the real atmosphere has very com-
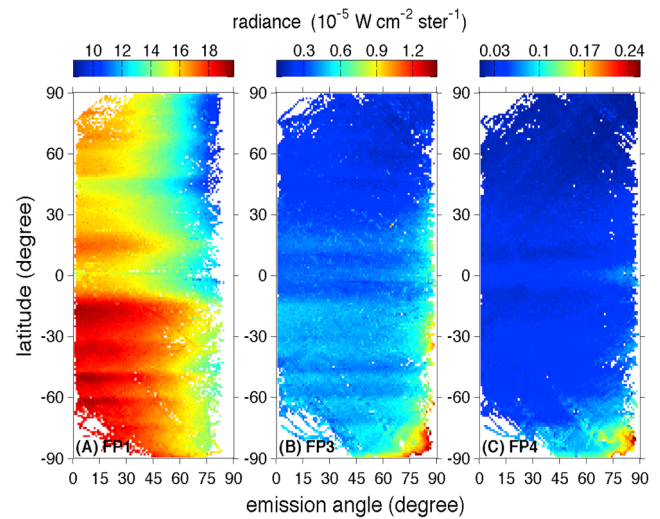

Figure 3. Temporal mean wave number-integrated radiance in the plane of latitude and emission angle for (a) FP1, (b) FP3, and (c) FP4, respectively. The temporal mean radiance is an average of all observations of Saturn's atmosphere between October 2004 and December 2009.
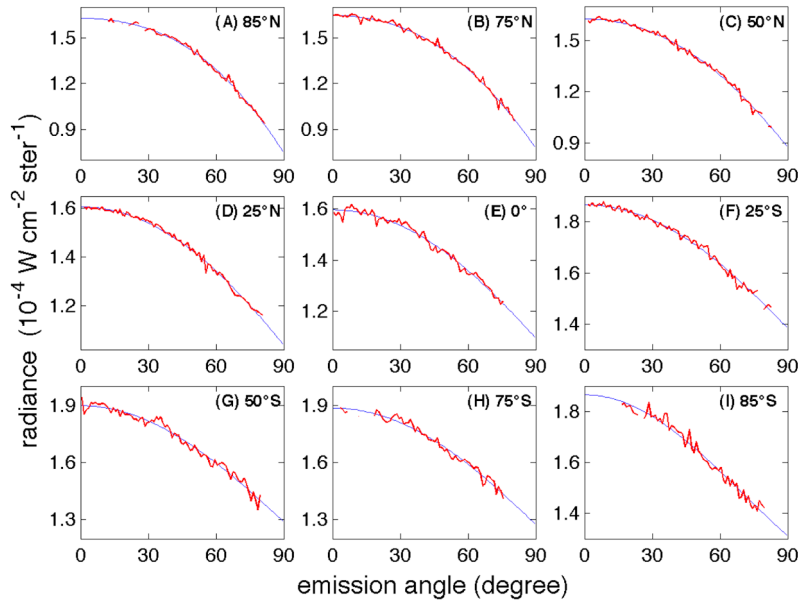
Figure 4. Least squares fitting of CIRS observations by the focal plane FP1 at different latitudes. Equation (5) in the text is used in the fitting. The red lines are observations, and the blue lines are fitting lines: (a) 85°N, (b) 75°N, (c) 50°N, (d) 25°N, (e) 0°, (f) 25°S, (g) 50°S, (h) 75°S, and (i) 85°S.

plicated thermal/dynamic structures. Here we use a least squares fit to interpolate/extrapolate from existing observations to unmeasured emission angles, enabling numerical integration. Figure 3 shows that radiance is a function of emission angle, so we define a fitting function with the following format,

$$I(\delta) = c_1 \cos^2 \delta + c_2 \cos \delta + c_3, \quad (5)$$

where c_1, c_2, and c_3 are coefficients, which are fitted to the observed radiance. Applying the least squares fit to a poly-nomial [*Bevington and Robinson*, 2003], we fit the observed radiance with equation (5) at all latitudes. Figures 4–7 show the results of fitting with equation (5) at different latitudes for each focal plane.

[15] Figure 4 shows the comparison of FP1 radiance as a function of emission angle between the observations and fitting results, which suggests that the least squares fit works well for FP1 observations. By examining the fitting coefficients (c_1, c_2, and c_3) at different latitudes, we find that the c_1 is roughly one order of magnitude smaller than c_2 for all altitudes, which suggests that the linear term ($c_2 \cos\delta$) is
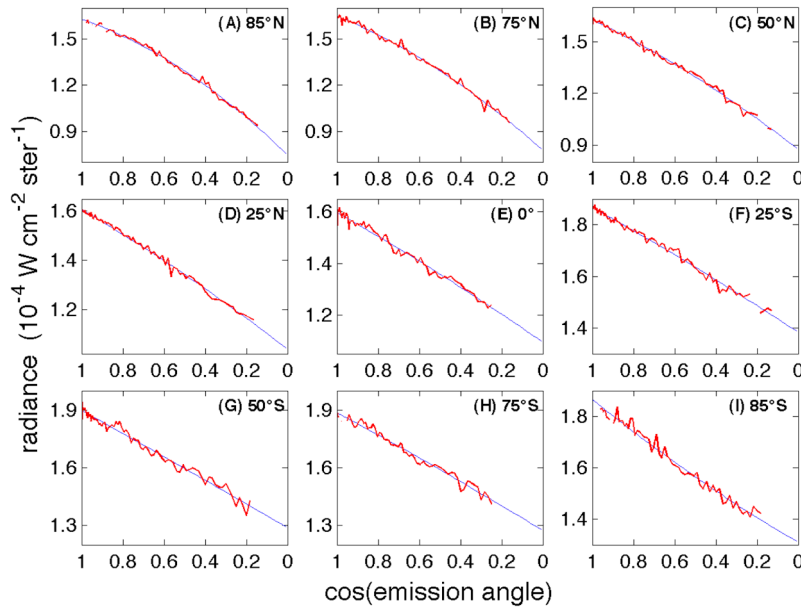

Figure 5. Same as in Figure 4, except for setting the cosine of emission angle instead of emission angle in the *x* axis.
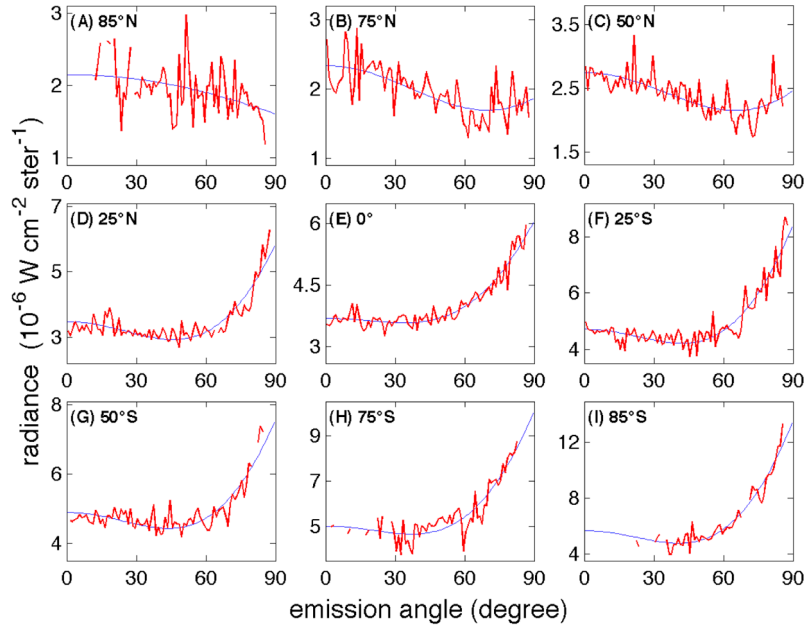
Figure 6. Same as in Figure 4, except for fitting the CIRS observations by the focal plane FP3.

dominant in the variance of radiance along the direction of emission angle. In addition, we also plot the radiance I varying with $\cos\delta$ instead of δ in Figure 5, which clearly shows a nearly linear relationship between the observed radiance (I) and the cosine of emission angle ($\cos\delta$) in the wave number range of FP1 (5–600 cm^{-1}). We also examine the fitting coefficients (c_1, c_2, and c_3) for the radiances recorded by FP3 and FP4, which are presented in Figures 6 and 7, respectively. We find that the coefficient c_1 of the quadratic term ($c_1 \cos^2\delta$) is the same magnitude as the coefficient c_2 of the linear term ($c_2 \cos\delta$) at most latitudes, suggesting that the variance of radiance along the direction

of emission angle is nonlinear in the wave number ranges of FP3 and FP4 (600–1430 cm^{-1}). The more complex variation of radiance in this spectral region is probably related to the gaseous emission/absorption bands.

[16] Figures 6 and 7 also show that the least squares fit is good except for high latitudes (60°N–90°N) of the NH. Fortunately, the radiance in the wave number range of FP3 and FP4 (605–1430 cm^{-1}) contributes a very small fraction of total thermal radiance (less than 2%). For the global mean thermal radiance, the high-latitude (60°N–90°N) radiance recorded by FP3 and FP4 contributes less than 0.2%. Therefore, the imperfect fitting of radiance in the high latitudes

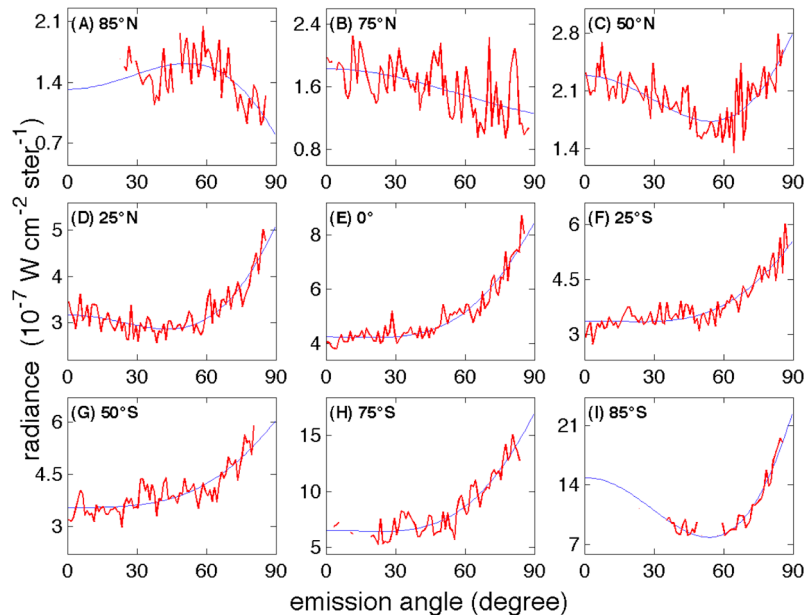**Figure 7.** Same as in Figure 4, except for fitting the CIRS observations by the focal plane FP4.

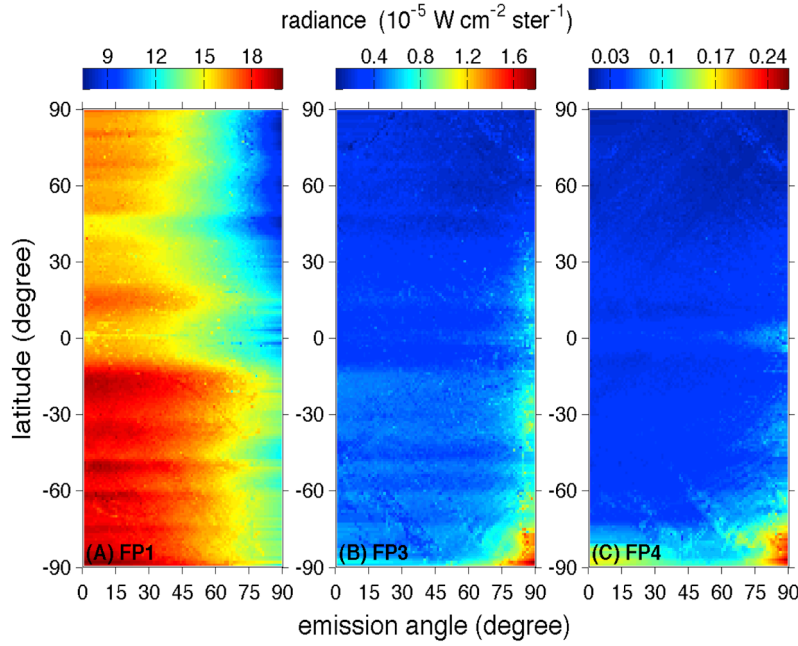radiance (10^{-5} W cm^{-2} ster^{-1})

Figure 8. Filling the observational gaps in Figure 3 with the least squares fitting. Shown is the radiance recorded by the focal plane (a) FP1, (b) FP3, and (c) FP4.

of the NH in this spectral region does not significantly affect our discussion of emitted power and energy balance of Saturn. However, the uncertainty due to filling the observational gaps by the least squares fit (including the imperfect fitting of radiance by FP3 and FP4 in high latitudes of the NH) is accounted for in our estimate of the uncertainty of emitted power.

[17] The fitting function with the known coefficients (c_1, c_2, and c_3) is utilized to fill the observational gaps in emission angle at all latitudes for the radiances recorded by each focal plane. The radiance after filling the observational gaps is shown in Figure 8. Figure 9 is the ratio of fitting residual to the raw radiance for these observational points, which highlights the difference between the observations and
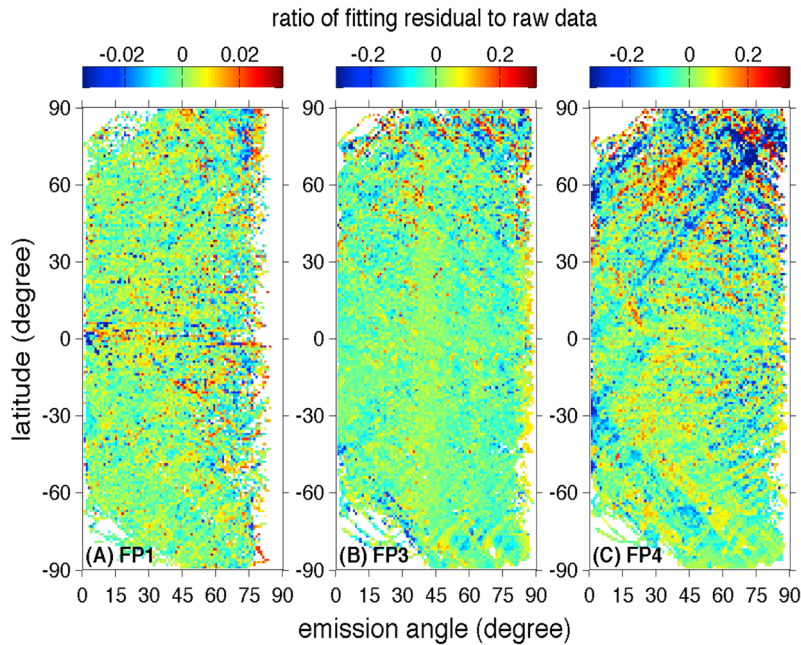
ratio of fitting residual to raw data

Figure 9. Ratio of fitting residual (fitting value − observational data) to the raw observational data. Figure 9 is based on Figures 3 and 8 for these points in the plane of latitude and emission angle where the CIRS observations are available: (a) FP1, (b) FP3, and (c) FP4.
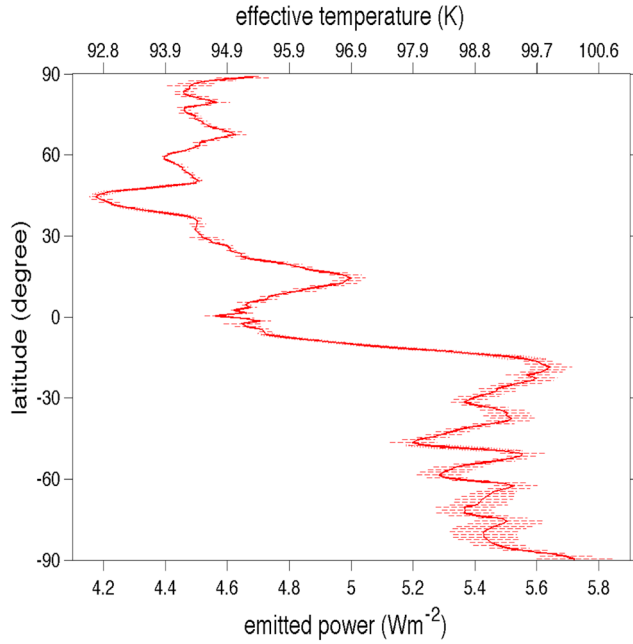
Figure 10. Meridional profile of temporal mean (2004–2009) emitted power and effective temperature. The solid line is the profile of emitted power and effective temperature, and the horizontal dashed lines represent the standard deviation of temporal variance.

the fitting results. Figure 9 shows that the ratio is less than 3% at all latitudes of FP1 (Figure 9a), which demonstrates again that the least squares fit works well for the FP1 radiance. The ratios are relatively larger in the higher latitudes of the NH in FP3 and FP4, but the imperfect fitting in these latitudes does not affect our evaluations of emitted power due to their small contribution, as discussed before. On the basis of the complete radiance in the plane of latitude and emission angle (Figure 8), we can calculate the meridional profiles of emitted power $P_{emit}(\phi)$ and the corresponding effective temperature $T_{eff}(\phi)$. Then the meridional distributions of emitted power and effective temperature are used to evaluate the average global emitted power and effective temperature ($\overline{P}_{emit}$ and $\overline{T}_{eff}$).

4.   Results

[18]   The mathematical framework described in section 2 and the CIRS data described in section 3 allowed us to evaluate the emitted power of Saturn and its meridional profile. The temporal mean (2004–2009) characteristic, seasonal variability, and interannual variability of emitted power and effective temperature of Saturn are now discussed.

4.1.   Time-Mean Characteristics

[19]   The temporal mean CIRS radiances (Figure 8) are utilized to calculate the temporal mean emitted power and effective temperature ($P_{emit}(\phi)$ and $T_{eff}(\phi)$). The meridional distribution of mean (2004–2009) emitted power and effective temperature is presented in Figure 10. The horizontal dashed lines in Figure 10 represent the standard deviation of temporal variation of emitted power and effective tempera-

ture during the period of 2004–2009. The most dominant feature shown in Figure 10 is the asymmetry of radiance between the southern and Northern Hemisphere, which is likely due to the summertime geometry of the SH versus the wintertime geometry of the NH during the time period of 2004–2009. The relatively small-scale oscillations of emitted power in the two hemispheres are related to the temperature structure in the troposphere of Saturn, which is displayed in Figure 11. The thermal structure of Saturn has important implications to the atmospheric dynamics, which has already been discussed in previous studies [*Flasar et al.*, 2005; *Li et al.*, 2008; *Read et al.*, 2009].

[20]   Figure 11 also shows that the profile of effective temperature matches well with the atmospheric temperature at 320 mbar in the SH, which suggests that the weighting function of the outgoing thermal radiance of Saturn is peaked near that level. In the NH, the profile of effective temperature sits between the 250 mbar profile and 320 mbar profile of atmospheric temperature. Some small structures of emitted power in the NH are similar with the profiles of the shallower atmosphere (200 mbar, 160 mbar, and shallower (not shown)), which suggests that the relatively shallow atmosphere (pressure < 200 mbar) also contributes to the outgoing thermal radiance in the NH. The different weighting functions of the outgoing thermal radiance between the SH and NH are probably due to the different vertical/meridional distributions of cloud/haze particles and the atmospheric chemical components causing the absorption/emission bands in the troposphere/stratosphere during the period of 2004–2009. The 10 year (1994–2003) observations from Hubble Space Telescope have already revealed time variation of cloud/haze structure in the SH of Saturn [*Perez-Hoyos et al.*, 2005]. The
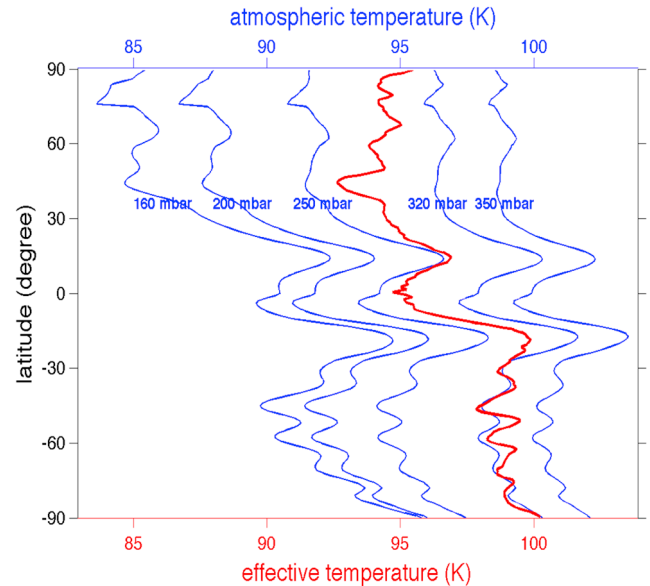

Figure 11. Comparison between the effective temperature and the atmospheric temperatures at different pressure levels. The red line is the temporal mean effective temperature between 2004 and 2009, which comes from the temporal mean emitted power. The blue lines are the temporal mean atmospheric temperatures of Saturn between 2004 and 2008 [*Li et al.*, 2008].

Table 2. Spatial Average of the Time Mean (2004–2009) Emitted Power and Effective Temperature[a]

	Global Average	NH Average	SH Average
Emitted power (W/m^2)	4.952	4.573	5.331
Standard deviation (W/m^2)	±0.035	±0.014	±0.058
Effective temperature (K)	96.67	94.77	98.47
Standard deviation (K)	±0.17	±0.07	±0.27

[a]The standard deviation of temporal variance listed here is based on the seasonal variance of emitted power and effective temperature during the period 2004–2009.

accumulating knowledge of the global distribution of cloud/haze particles and atmospheric chemical components during the epoch of Cassini (2004–), combined with radiation models, will help us to interpret the different weighting function between the SH and NH.

[21] The meridional distribution of emitted power ($P_{emit}(\phi)$) and equation (3) was integrated to evaluate the hemispheric and global averages of emitted power, and corresponding effective temperatures were computed by equation (4). These are presented in Table 2, along with the standard deviation of the temporal variance during the period of 2004–2009, showing that the emitted power and effective temperature are higher in the SH than in the NH by 16.6% and 3.9%, respectively.

4.2. Seasonal Variability

[22] Besides the temporal-mean emitted power and effective temperature between 2004 and 2009, we also explore the temporal variations of emitted power and effective tempera-

ture from 2004 to 2009. Figure 12 shows the coverage of CIRS observations by FP1 in the plane of latitude and emission angle at different Earth years. The observed radiance is sparse in the plane of latitude and emission angle in 2004 and 2005 (less than 30% of the total areas of the plane of latitude and emission angle), but they help to improve the coverage of radiance in 2006. Therefore, the CIRS observations in 2004 and 2005 are combined with the observations in 2006 (Figure 11a). Figure 12 only shows the coverage of radiance recorded by FP1. The coverage of radiance recorded by FP3 and FP4, which is a little better than the coverage of radiance by FP1 (Figure 11), is not shown.

[23] As with the time averaged data, we use the least squares fit, which is based on equation (5), to fill the observational gaps in the planes of latitude and emission angle. Then we calculate the emitted power at different Earth years between 2004 and 2009, presented in Figure 13, and showing noticeable variation of emitted power and effective temperature in the SH from 2004 to 2009. The difference of emitted power and effective temperature between the neighboring years is larger than the uncertainties within each year, so the temporal variations from 2004 to 2009 shown here are real. The uncertainties for each year, which include errors from calibration and least squares fitting, are discussed in section 5. The estimated uncertainties shown here are different from the standard deviation of temporal change shown in Figure 11. Figure 13 also shows that the temporal variation of emitted power and effective temperature in the NH is not noticeable for most latitudes. However, the following discussion shows that the corresponding hemispherically averaged quantities have significant temporal variations for both the SH and NH.
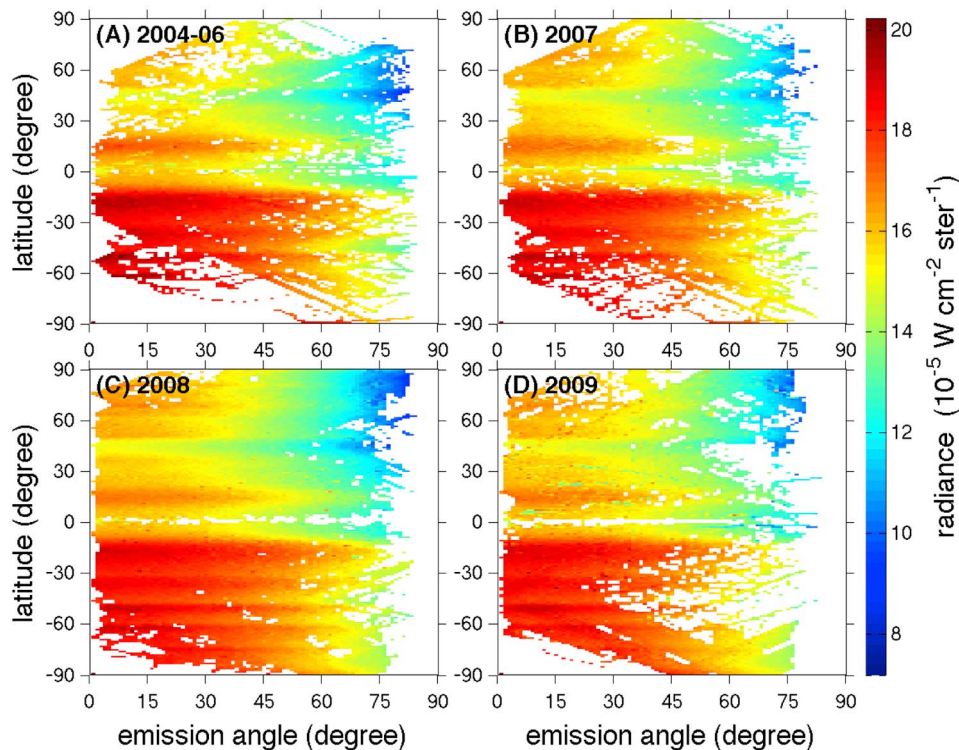

Figure 12. Coverage of CIRS radiance in the plane of latitude and emission at different Earth years. The CIRS radiance shown here is observed by the focal plane FP1: (a) radiance between 2004 and 2006, (b) radiance in 2007, (c) radiance in 2008, and (d) radiance in 2009.
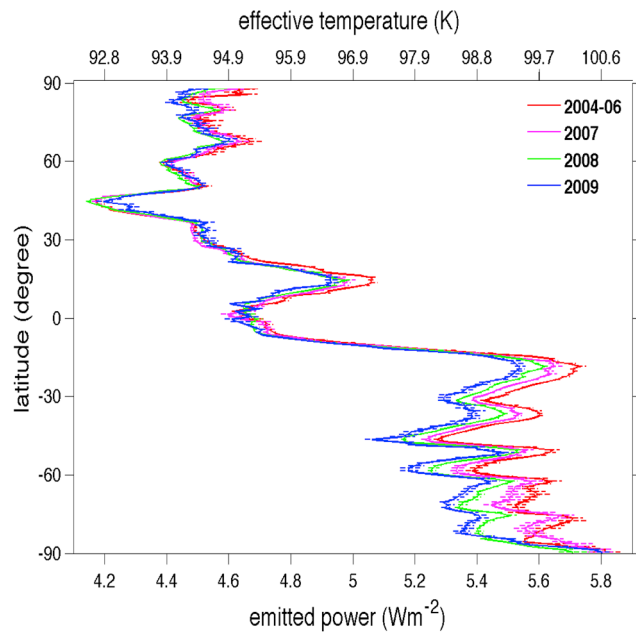
Figure 13. Temporal variation of emitted power and effective temperature between 2004 and 2009. The lines in color are the meridional profiles of emitted power and effective temperature at different Earth years. The horizontal dashed lines are the corresponding uncertainty.

[24] Figures 14 and 15 show the temporal variation of global/hemispheric average emitted power and effective temperature from 2005 to 2009. The corresponding solar longitude changes from ~299.7° at the beginning of 2005 to ~4.9° at the end of 2009. Here the solar longitude is defined as the longitude of the Sun on the sky in a Saturn centered, ecliptic reference frame, with the zero of longitude at northern spring equinox. Figure 14 shows that the global emitted power decreases by ~2% from ~5.0 W m^{-2} in 2005 to ~4.9 W m^{-2} in

2009. The corresponding effective temperature decreases by ~0.5% from ~96.9 K in 2005 to ~96.5 K in 2009. This variation of emitted power is related to the seasonal variation of tropospheric temperature [*Fletcher et al.*, 2010], which is mainly controlled by the temporal variation of solar radiance at each latitude. In addition, the temporal evolution of cloud/haze structure [*Perez-Hoyos et al.*, 2005] and the associated variation in the deposition of solar flux [*Perez-Hoyos and Sanchez-Lavega*, 2006] probably affect the seasonal variation of atmospheric temperature and hence emitted power on Saturn.

[25] Figure 15a shows that the emitted power decreased from 2005 to 2008 in the NH and increased from 2008 to 2009 as the northern vernal equinox (solar longitude = 0°) arrived in August 2009. The NH received constantly increasing solar radiance during the time period of 2005–2009. However, the emitted power in the NH does not show the increasing trend corresponding to the increasing solar radiance until 2008, probably because the long radiative time constant of the atmospheric layers involved in the emitted power (~24 Earth years) [*Conrath et al.*, 1989] results in the response of emitted power that lags the solar forcing by a few Earth years. Panel B shows that the emitted power in the SH decreases by ~3.0% from ~5.41 W m^{-2} in 2005 to ~5.25 W m^{-2} in 2009. The corresponding effective temperature of the SH decreases by ~0.8% from ~98.83 K in 2005 to ~98.08 K in 2009. Figure 15b also shows that the decreasing trend of emitted power and effective temperature becomes stronger after 2008. The Cassini Solstice Mission will provide us with improved information about the seasonal variation of emitted power and effective temperature on Saturn.

4.3. Interannual Variability

[26] The solar longitude in the epoch of Saturn flyby by Pioneer 11 (1979) is 353.6°, and the solar longitude in the epoch of Saturn flyby by Voyager 1 and 2 (1980 and 1981) is 8.6° and 18.2°, respectively. The solar longitudes in the epochs of Pioneer and Voyager are roughly 1 Saturn year
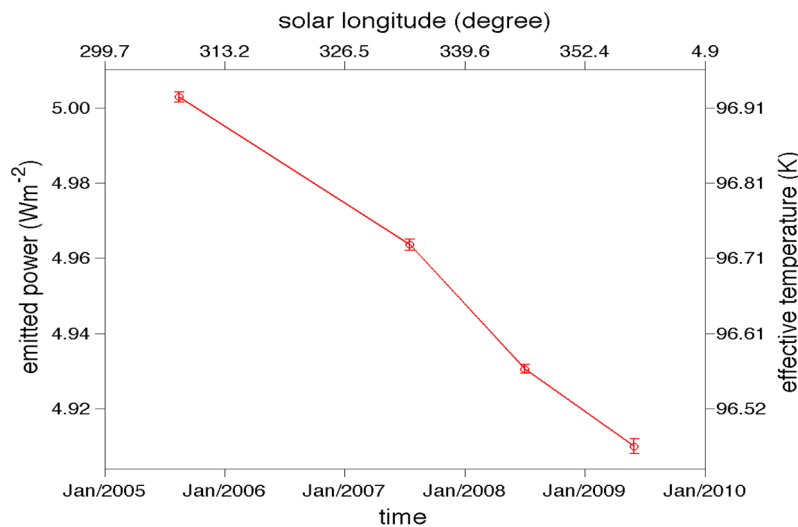

Figure 14. Temporal variation of global emitted power and effective temperature between 2004 and 2009. The times of the points are the average of observational times over the corresponding time periods. The error bars, which include the uncertainty related to calibration and filling observational gaps, are discussed in section 5.
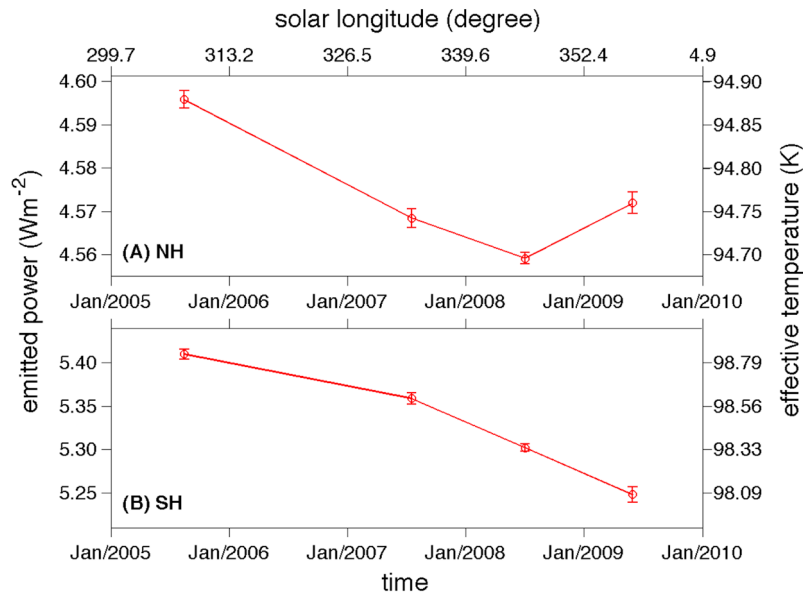
Figure 15. Temporal variation of emitted power and effective temperature in the two hemispheres between 2004 and 2009: (a) Northern Hemisphere (NH) and (b) Southern Hemisphere (SH).

(~29.4 Earth years) before the current epoch of Cassini from 2004 to 2009 with solar longitude varying from 296.8° to 4.9°. Therefore, we can compare the current study with the Pioneer/Voyager studies to explore possible interannual variability of emitted power and effective temperature. The meridional distribution and spatial average of emitted power and effective temperature were both evaluated from the observations by Voyager 1 and 2 [*Hanel et al.*, 1983; *Conrath and Pirraglia*, 1983; *Ingersoll*, 1990]. The average global emitted power and effective temperature were also presented in the study of the observations by Pioneer 11 [*Ingersoll et al.*, 1980; *Orton and Ingersoll*, 1980].

[27] Figure 16 shows the comparison of the meridional profile of emitted power and effective temperature between the observations by Voyager 1 and 2 in 1980–1981 [*Conrath and Pirraglia*, 1983; *Ingersoll*, 1990] and the observations by Cassini in 2009. The average solar longitude in 2009 is 357.4°, which is close to the average solar longitude 13.4° in 1980–1981. The significant asymmetry of emitted power and effective temperature between the two hemispheres (Figure 16, red line), which is detected in 2009 by Cassini, is not apparent in the 1980–1981 observations by Voyager (Figure 16, blue line). For the NH, the strong maximal peak at ~30°N in the epoch of Voyager seems to disappear in the epoch of Cassini. The minimal peak at ~15°N changed into a maximal peak from 1980–1981 to 2009. For the other latitudes of the NH, the Voyager profile has roughly the same distribution as Cassini's, but with offsets ~0.3 W m^{-2} and ~1 K in emitted power and effective temperature, respectively. Figure 16 also shows that the Cassini profile is the same as the Voyager 1 in the SH but with offsets ~0.8 W m^{-2} and ~4 K in emitted power and effective temperature, respectively. In addition, the high-resolution (1° in latitude) Cassini profile displays some fine structure, which was not resolved by the previous studies. The difference of emitted power and effective temperature in the meridional direction between the two epochs is much larger than the uncertainty in
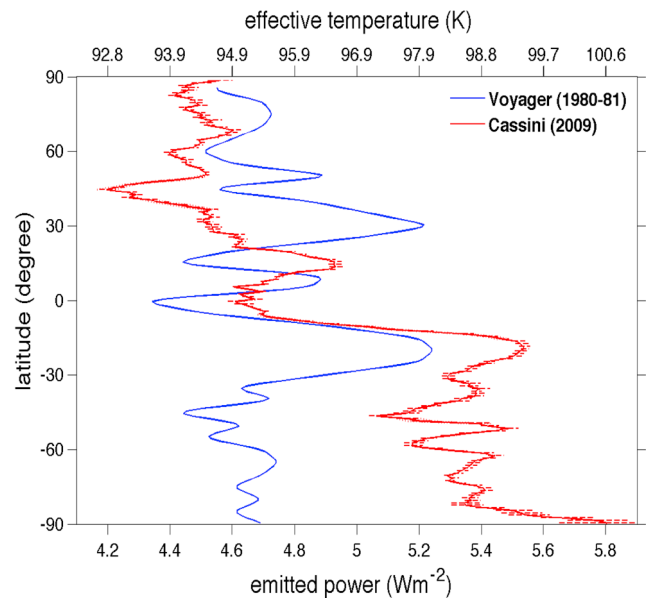

Figure 16. Comparison of meridional distribution of emitted power and effective temperature between the epoch of Voyager and the epoch of Cassini. The observations by Voyager 1 and 2 were conducted in November 1980 and August 1981, respectively. The corresponding solar longitudes are 8.6° and 18.2°, respectively. The observations by Cassini were conducted over the whole year of 2009. The average of the observational times is 28 May 2009, which corresponds to solar longitude 357.4°. The red horizontal dashed lines show the uncertainty, which is discussed in section 5, for the results of Cassini. There are no estimates of uncertainty for the meridional profile of Voyager available in the previous studies.

Table 3. Global Values of Emitted Power and Effective Temperature by Spacecrafts Pioneer, Voyager, and Cassini[a]

	Pioneer 11	Voyager 1	Cassini
Time	September 1979	November 1980	May 2009
Solar longitude (°)	353.6	8.6	357.4
Emitted power (W/m^2)	4.91	4.614	4.9108
Uncertainty (W/m^2)	±0.50	±0.075	±0.0048
Effective temperature (K)	96.5	95.00	96.470
Uncertainty (K)	±2.5	±0.4	±0.023

[a]The global values of Pioneer come from the study by *Orton and Ingersoll* [1980], in which some simplifying assumptions are made on the measurements between 30°S and 10°N. The global values of Voyager come from the study by *Hanel et al.* [1983]. The other studies, which are based on Earth-based and airborne telescopes, are not included here because of the relatively large uncertainty and the discrepancy between them.

the Cassini results (Figure 16, horizontal dashed lines). The uncertainty of the meridional profile of emitted power and effective temperature in the epoch of Voyager was not available in the previous studies. The estimated uncertainties of these quantities in the epoch of Voyager [*Hanel et al.*, 1983] are 0.075 W m^{-2} and 0.8 K, respectively. It seems that the difference of emitted power and effective temperature between the Voyager profile and the Cassini profile is due to interannual variability, if we assume that the uncertainty at each latitude is in the same order of magnitude of the estimated uncertainty of the global average values in the epoch of Voyager. The solar longitude of Saturn in September of 2010 will be same as the average solar longitude during the Voyager encounter (13.4°). The relativity small changes between 2004 and 2009 (Figure 15) suggest that the emitted power and effective temperature cannot reach the levels of Voyager profile in the year of 2010 unless variability suddenly increases.

[28] The global average emitted power and effective temperature observed by Pioneer, Voyager, and Cassini are displayed in Table 3. The estimated uncertainty decreases roughly 1 order of magnitude from Pioneer to Voyager and from Voyager to Cassini. Let us first compare the Cassini results with the previous best estimates from Voyager [*Hanel et al.*, 1983]. Figure 12 shows that the emitted power decreased ~0.023 W m^{-2}/yr for the emitted power and ~0.015 K/yr for the effective temperature during the time period of 2005–2009. Extrapolating from the changing rate in 2005–2009, the emitted power (effective temperature) will be ~4.89 W m^{-2} (~96.32 K) in 2010. The solar longitude in 2010 is roughly same as that in the epoch of Voyager. The predicted emitted power and effective temperature in 2010 is larger than the values of Voyager in 1980 [*Hanel et al.*, 1983] by ~0.28 W m^{-2} (~6.0%) and ~1.32 K (~1.4%). The predicted interannual changes between Voyager and Cassini is larger than the estimated uncertainty and will be looked for in the Cassini extended mission.

[29] By the comparison between the Pioneer and Cassini results, which are in the roughly same season (Table 3), we find that the emitted power and effective temperature are basically the same. On the basis of the Pioneer measurements between 30°S and 10°N, *Orton and Ingersoll* [1980] made some simplifying assumptions for other latitudes to estimate the average global emitted power and effective temperature. Therefore, the corresponding uncertainties are much larger (±0.50 W m^{-2} and ±2.5 K for emitted power and effective temperature, respectively). Such uncertainties are larger than

the predicted interannual variability between the Voyager and Cassini epochs (0.28 W m^{-2} and 1.32 K for emitted power and effective temperature, respectively). Therefore, it is still possible that the interannual variability is real.

[30] There are some possible reasons for the interannual variability of emitted power and effective temperature among the three epochs of Pioneer, Voyager, and Cassini. First, the solar flux at the top of Saturn's atmosphere is different among these epochs. The solar flux varies ~0.1% with different solar cycles (~11 Earth years) [*Lean and Rind*, 2009]. Therefore, we utilize the average solar flux from previous studies [*Esposito et al.*, 1984; *Barnet*, 1990; *Dones et al.*, 1993; *Perez-Hoyos and Sanchez-Lavega*, 2006] to estimate the solar flux in the three epochs. Figure 17 displays the meridional profiles of solar flux at the top of Saturn's atmosphere at each era. The solar flux displays more significant asymmetry between the two hemispheres at the time of Voyager than at the time of Cassini, which is the opposite trend to Figure 16 in which the emitted power displays more asymmetry in the Cassini epoch than in the Voyager epoch. Therefore, the solar flux cannot explain the different meridional profiles of emitted power and effective temperature between the two times. The second possible reason is the rings' effects (i.e., blocking solar radiance, reflecting/scattering solar radiance, and the thermal emission onto Saturn). Considering that the rings' effects are concentrated in the equatorial region of Saturn and the relative geometry between the rings and Saturn are roughly same between the Voyager and Cassini investigations, the temporal variation of rings' effects between the two epochs will not be significant if the albedo and temperature of rings does not change greatly. The final possible reason is the interannual variability of cloud/haze structure and the associated deposit of solar flux. The varying cloud/haze structure can change the thermal structure of atmosphere and hence the
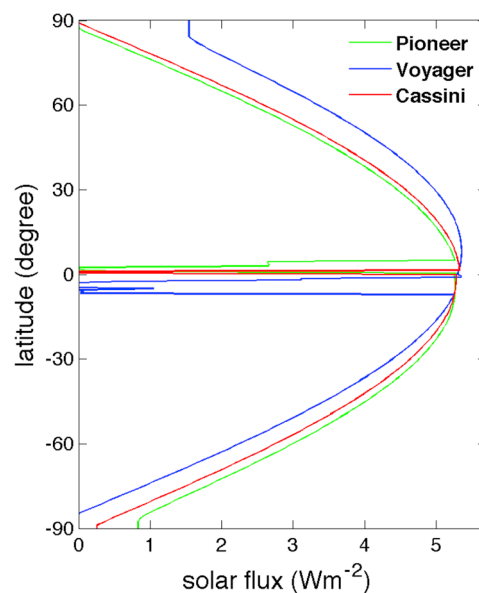

Figure 17. Solar flux at the top of Saturn's atmosphere given as a function of latitude. The data come from Figure 1 of *Perez-Hoyos and Sanchez-Lavega* [2006] with solar longitudes of 353.6°, 13.4°, and 357.4° for Pioneer, Voyager, and Cassini, respectively.
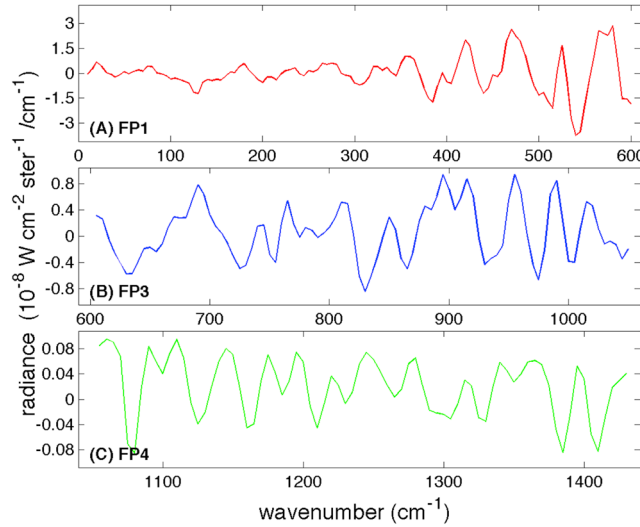
Figure 18. Typical CIRS spectra recorded by the three focal planes (a) FP1, (b) FP3, and (c) FP4 when viewing deep space. The spectra were taken by CIRS in the middle of 2007 with spectral resolution 15.5 cm^{-1}.

emitted power/effective temperature. The interannual cloud variability on Jupiter has already been discovered [*Baines et al.*, 2007]. Therefore, the interannual variation of emitted power and effective temperature discussed in this study implies that there is the inter-annul variability of cloud/haze structure and deposit of solar flux on Saturn besides their seasonal variation [*Perez-Hoyos et al.*, 2005; *Perez-Hoyos and Sanchez-Lavega*, 2006].

5. Uncertainty Estimate

[31] In this study, the Cassini/CIRS spectra are analyzed to calculate the emitted power and effective temperature. Therefore, the uncertainty of the CIRS spectra, which is related to the calibration of the spectra, is a critical topic. Here we discuss the uncertainties due to calibration and also due to the filling of observational gaps by least squares fitting.

5.1. Uncertainty Related to Calibration

[32] The basic approach for the calibration of the CIRS measurements to absolute radiance of target (i.e., Saturn) follows the techniques described in some previous studies [*Flasar et al.*, 2004; *Hanel et al.*, 1980, 2003]. The main process of CIRS calibration is to remove the radiance of the background (i.e., the instrument itself) from the radiance of the target, and to account for the spectral response of the detectors. To estimate the background radiance, the spectrometer routinely views deep space (i.e., zero radiance from target). Figure 18 displays the typical calibrated spectra recorded by the three focal planes (FP1, FP3, and FP4) when viewing deep space. The absolute radiometric calibration is accomplished differently for FP1, which operates at the 170 K instrument temperature, and FP3 and FP4, which are cooled to ~75 K. For FP1, it is implicitly assumed that the instrument has zero signal when viewing a 170 K target, so only a 2.7 K deep space reference is required to find the responsivity, assumed linear. For FP3 and FP4, a second reference target

is required to determine the instrument background (self-emission), which is a 170 K shutter that is periodically inserted into the field. For further details of radiometric calibration, see *Flasar et al.* [2004], Appendix C, and references therein. A discussion of the temporal stability of the FP1 detector can be found in the work of *Brasunas and Lakew* [2004]. Comparing with the radiance of Saturn shown in Figure 1, Figure 18 shows that the background noise is smaller than the radiance of Saturn by roughly two orders of magnitude. The uncertainty related to the background noise in the spectral ranges 10–600 cm^{-1} (FP1), 605–1050 cm^{-1} (FP3), and 1055–1430 cm^{-1} (FP4) is estimated as follows: we randomly choose ~100,000 spectra of deep space for each year of 2004–2009. These are first integrated in wave number (10–1430 cm^{-1}) because the spectra of Saturn are integrated when calculating the emitted power. The mean value and standard deviation of these ~100,000 wave number-integrated spectra are used as an estimator for the uncertainty due to the background radiance in each year. The mean value and the standard deviation of these are listed in Table 4, showing that the standard deviation is larger than the mean by one order of magnitude. We add the absolute mean value to the standard deviation to estimate the calibration error of emitted power for each Earth year. This is added to the uncertainty due to filling observational gaps.

[33] Currently, there are two main calibration methods for CIRS spectra. The first method is to find the radiance of the nearest block of deep space (in time) to the target observation to evaluate the background radiance. The second method is to use a "grand average" of all radiance of deep space across the whole tour. Figure 19 presents a comparison of emitted power in 2007 between the two methods. The two meridional profiles in Figure 19 match each other very well, which suggests that the variation of background radiance due to calibration method is not very important. Therefore, the analyses in this study, based on the CIRS data with the first calibration method, are not significantly affected by using different CIRS data sets with different methods of calibration.

5.2. Uncertainty Related to Filling Observational Gaps

[34] The other uncertainty of emitted power and effective temperature is related to filling observational gaps by the least squares fit. The sum of unknown radiance in the observational gaps along a single latitude can be expressed as

$$P_{\text{emit}}(N) = 2\pi \sum_{k=1}^{N} I(\delta_k) \cos \delta_k \, \sin \delta_k \Delta \delta = \sum_{k=1}^{N} c_k I_k, \quad (6)$$

where the coefficient c_k is represented by $c_k = 2\pi\Delta\delta\cos\delta_k\sin\delta_k$ and N is the number of these unknown radiances (i.e., observational gaps) along the latitude. Therefore, the difference

Table 4. Mean Value and Standard Deviation of Background Noise[a]

	Year						Unit
	2004	2005	2006	2007	2008	2009	
Mean	0.96	2.65	−1.51	4.11	−0.98	1.55	10^{-4} W m^{-2}
Standard deviation	2.93	2.67	4.15	4.04	3.63	3.42	10^{-3} W m^{-2}

[a]The mean values and standard deviation are based on ~100,000 wave number-integrated radiance of calibrated deep space for each Earth year.
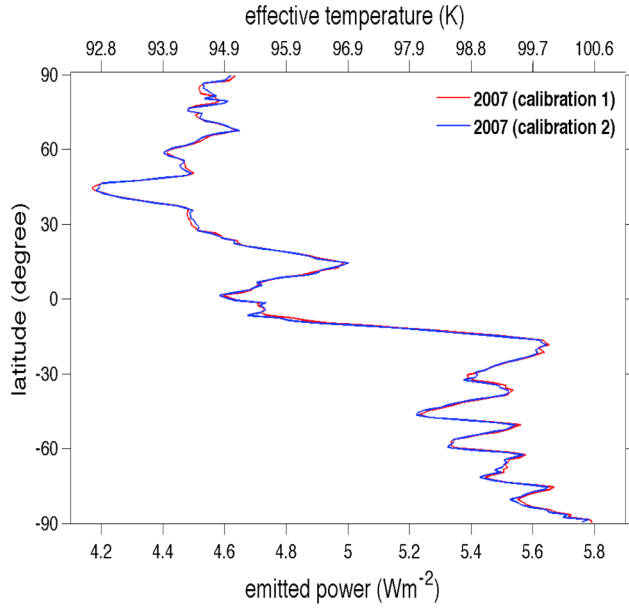
Figure 19. Comparison of emitted power between method 1 and method 2 of calibration.

between the fitting radiance and the real radiance for these observational gaps can be written as

$$P_{emit}(N)' = \sum_{k=1}^{N} c_k I_k', \qquad (7)$$

where $P_{emit}(N)'$ is the total difference, which is the sum of the radiance difference I_k' at each unknown point. The variance of $P_{emit}(N)'$ is used to estimate the uncertainty of emitted power related to filling the observational gaps and is determined by the variance and covariance of the radiance difference I_k' at the observational gaps [*Bevington and Robinson*, 2003, pp. 42–43],

$$\sigma^2\left(P_{emit}(N)'\right) = \sum_{k=1}^{N} c_k^2 \sigma_k^2 + 2 \sum_{i=2}^{N} \sum_{j=1}^{i-1} c_i c_j \sigma_{ij}^2, \qquad (8)$$

where σ_k^2 is the variance of each radiance difference I_k' and σ_{ij}^2 is the covariance of the radiances at two different unknown points. Our previous discussion shows that the least squares fit does a good job of fitting the radiance recorded by FP1, which dominates the emitted power of Saturn. The residual of fitting curves to the observational data is used to estimate the variance of the radiance difference σ_k^2 at the observational gaps. The covariance σ_{ij}^2 will disappear if we assume that the radiances at different unknown points are independent from each other. It is indeed possible that the unknown radiances are correlated with each other; however, we are compelled to neglect the covariance because we do not have a good way to estimate it. Neglecting the covariance, we have

$$\sigma^2\left(P_{emit}(N)'\right) = \sum_{k=1}^{N} c_k^2 \sigma_k^2. \qquad (9)$$

Equation (9) is utilized to estimate the uncertainty of emitted power from these unknown radiances (i.e., observational

gaps) along the each latitude. Our estimate shows that such uncertainty is larger than the uncertainty related to the CIRS calibration by roughly one order of magnitude. We combine the two uncertainties as the total uncertainty of emitted power at each Earth year during the time period of 2004–2009, shown by the error bars along the profiles in Figure 13.

[35] The combined uncertainty of emitted power from calibration and filling observational gaps at each Earth year, shown in Figure 13, is much smaller than the standard deviation of temporal variance during the time period of 2004–2009, shown in Figure 10. Figure 20 further displays the comparison of the combined uncertainty and the standard deviation of emitted power during 2004–2009, clearly suggesting that the standard deviation of temporal variance (Figure 20b) is larger than the combined uncertainty from random and systematic errors (Figure 20a) by one order of magnitude. Therefore, the seasonal variation of emitted power and effective temperature from 2004 to 2009, discussed in section 4.2, is robust. Figure 20a also shows that the uncertainty is larger in the polar region than at other latitudes because the uncertainty from filling observational gaps is roughly proportional to the number of observational gaps. Figure 20b shows that standard deviation is larger in the SH than the NH due to larger seasonal changes (Figure 13).

[36] Having estimated the uncertainty of emitted power at all latitudes, we now discuss how to evaluate the uncertainty of spatial average emitted power. Here we use the average global emitted power as an example. Equation (3) can be rewritten as

$$\overline{P}_{emit} = \frac{1}{2(1 - 2\varepsilon/3)} \sum_{k=1}^{N=180} \left(1 - 2\varepsilon \sin \phi_k'\right) P_{emit}\left(\phi_k'\right) \cos \phi_k' \Delta \phi'$$

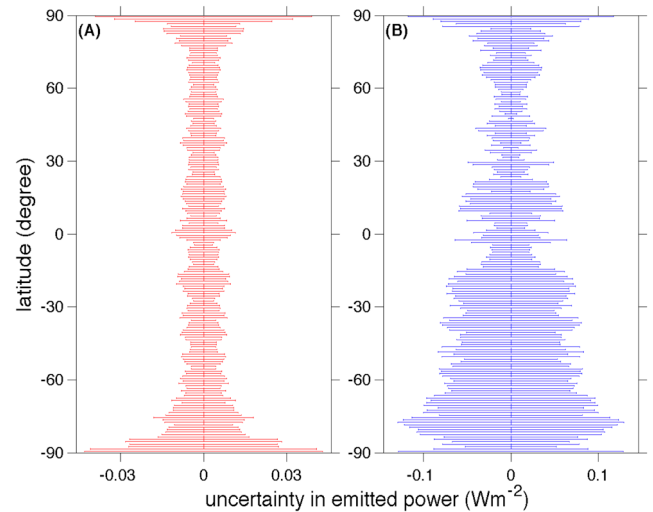$$= \sum_{k=1}^{N=180} c_k' P_{emit}\left(\phi_k'\right), \qquad (10)$$

Figure 20. Combined uncertainty of emitted power versus the standard deviation of temporal variance of emitted power. (a) Combined uncertainty from CIRS calibration and filling observational gaps, which is averaged over the time period of 2004–2009. (b) Standard deviation of the temporal variance of emitted power from 2004 to 2009, which is based on the profiles at different Earth years shown in Figure 13.

where coefficient c_k' is represented by $c_k' = [(1 - 2\varepsilon\sin\phi_k')$ $\cos\phi_k'\Delta\phi']/[2(1 - 2\varepsilon/3)]$. The index N is the number of latitude bands from pole to pole. The spatial resolution in the direction of latitude is $1°$ in this study, so we have the index N changing from 1 to 180. After converting equation (3) into equation (10), we can use equation (9) again to estimate the uncertainty of average global emitted power because the uncertainty of emitted power at all latitudes has already been estimated (Figure 12). The calculated uncertainty for the spatial average of emitted power and effective temperature is shown by the error bars in Figures 14 and 15 and Table 3.

6. Conclusion and Discussion

[37] The spectra of Saturn observed by Cassini/CIRS during the period of 2004–2009 are systematically analyzed to evaluate the emitted power and effective temperature of Saturn. The CIRS observations over nearly all viewing angles make it possible to precisely measure the meridional distributions of emitted power and effective temperature, which reveal a significant asymmetry between the two hemispheres of Saturn. The long-term CIRS observations also show that the average global emitted power and effective temperature decrease ~2% and ~0.5%, respectively, from 2005 to 2009. The comparison of the meridional distribution of emitted power and effective temperature between the Voyager and Cassini epochs suggests substantial interannual variability. Our study also predicts internal annual variability of global average emitted power and effective temperature between the epoch of Voyager and the forecast for Cassini at the same season (2010), which will be examined during the extended mission of Cassini.

[38] The temporal variation of emitted power and effective temperature on Saturn has never been observed. The time separation between Pioneer and Voyager is ~1–2 Earth years, which makes it possible to explore the seasonal variation of emitted power and effective temperature. However, the uncertainty of estimated emitted power and effective temperature due to the limitation of flyby observations is larger than the difference of emitted power and effective temperature between Pioneer and Voyager (Table 3), which makes it difficult to reach any robust conclusion. In addition, all previous observations of Saturn's emitted power and effective temperature were within one Saturn year (~29.4 Earth years) so that the interannual variability could not be explored prior to Cassini. Therefore, scientists assumed that the emitted power and energy balance on the giant planets are constant with time in all of previous and current studies. In this way, the seasonal and interannual variability of the quantities discovered by Cassini was unforeseen. The seasonal variation is probably related to the time evolution of atmospheric temperature and the structure of cloud/haze, and the interannual variation implies a temporal evolution of cloud/haze structure and variations in the deposition of solar flux between Saturn years.

[39] The seasonal and interannual variation of emitted power and effective temperature further implies time variability of energy balance and hence internal heat, which would occur if the time variation of absorbed solar radiance can not exactly compensate the time variation of emitted power. The evaluation of the absorbed solar radiance, based on observations by Cassini ISS and VIMS, is still in process.

The complicated effects of rings in both thermal radiance and solar radiance will be considered when evaluating the energy balance of Saturn, by following the theoretical framework presented in the study of *Hanel et al.* [1983]. The new results from observations by Cassini will be compared to the measurements from Pioneer and Voyager to explore the possible interannual variability of energy balance and internal heat for Saturn. In addition, the long-term observations by Cassini will make it possible to explore the seasonal variability of energy balance and internal heat.

[40] The potential time variation of energy balance and hence internal heat has important implications for these previous and current studies, which assumed that the energy balance and internal heat on the giant planets are constant with time: these should now be reexamined if the time variation is confirmed. The meridional distribution of energy balance and internal heat also has important consequences. One of our previous studies [*Li et al.*, 2006] assumed that the internal heat and the related moist convection are concentrated in the latitudes of cyclonic shear in the zonal wind on Jupiter and Saturn. Other model studies assume that the internal heat and related convection are randomly or uniformly distributed over the outer planets [*Busse*, 1976, 1983; *Christensen*, 2001; *Heimpel and Aurnou*, 2007; *Aurnou et al.*, 2007; *Chan and Mayr*, 2008; *Schneider and Liu*, 2008]. The new measurements by Cassini will shed light on these assumptions of spatial distribution of internal heat.

References

Aumann, H. H., C. M. Gillespi, and F. J. Low (1969), Internal powers and effective temperatures of Jupiter and Saturn, *Astrophys. J.*, *157*, L69–L72.

Aurnou, J., M. Heimpel, and J. Wicht (2007), The effects of vigorous mixing in a convective model of zonal flow on the ice giants, *Icarus*, *190*, 110–126.

Baines, K. H., et al. (2007), Polar lightning and decadal-scale cloud variability on Jupiter, *Science*, *318*, 226–229.

Barnet, C. D. (1990), Saturn's seasonal winds and temperature: The effect of the ring system on the troposphere and stratosphere, Ph.D. thesis, New Mexico State Univ., Las Cruces.

Bender, M. L., P. W. Callaway, S. C. Chase, G. F. Moore, and R. D. Ruiz (1974), Infrared radiometer for Pioneer 10 and 11 Missions to Jupiter, *Appl. Optics*, *13*, 2623–2628.

Bevington, P. R., and D. K. Robinson (2003), *Data Reduction and Error Analysis for the Physical Sciences*, 3rd ed., McGraw-Hill, New York.

Brasunas, J. C., and B. Lakew (2004), Long-term stability of the Cassini Fourier transform spectrometer en route to Saturn, *Recent Res. Devel. Opt.*, *4*, 95–113.

Busse, F. H. (1976), Simple model of convection in the Jovian atmosphere, *Icarus*, *29*, 255–260.

Busse, F. H. (1983), A model of mean zonal flows in the major planets, *Geophys. Astrophys. Fluid. Dyn.*, *23*(2), 153–174.

Chan, K. L., and H. G. Mayr (2008), A shallow convective model for Jupiter's alternating wind bands, *J. Geophys. Res.*, *113*, E10002, doi:10.1029/2008JE003124.

Chandrasekhar, S. (1950), *Radiative Transfer*, Oxford Univ. Press, London.

Christensen, U. R. (2001), Zonal flow driven by deep convection in the major planets, *Geophys. Res. Lett.*, *28*(13), 2553–2556, doi:10.1029/2000GL012643.

Conrath, B. J., R. A. Hanel, and R. E. Samuelson (1989), Thermal structure and heat balance of the outer planets, in *Origin and Evolution of*

Planetary and Satellite Atmospheres, edited by S. K. Atreya et al., Univ. of Arizona Press, Tucson, Ariz.

Conrath, B. J., and J. A. Pirraglia (1983), Thermal structure of Saturn from Voyager infrared measurements: Implications for atmospheric dynamics, *Icarus*, 53, 286–292.

Courtin, R., P. Lena, M. D. Muizon, D. Rouan, C. Nicollier, and J. Wijnbergen (1979), Far-infrared photometry of Planets: Saturn and Venus, *Icarus*, 38, 411–419.

Dones, L., J. N. Cuzzi, and M. R. Showalter (1993), Voyager photometry of Saturn's A ring, *Icarus*, 105, 184–215.

Erickson, E. F., D. Goorvitch, J. P. Simpson, and D. W. Strecher (1978), Far-infrared spectrophotometry of Jupiter and Saturn, *Icarus*, 35, 61–73.

Esposito, L. W., J. N. Cuzzi, J. B. Holberg, J. B. Marouf, G. L. Tyler, and C. C. Porco (1984), Saturn's rings: Structure, dynamics and particle properties, in *Saturn*, edited by T. Gehrels and M. S. Matthews, pp. 463–545, Univ. of Arizona Press, Tucson.

Flasar, F. M. (1973), Gravitational energy sources in Jupiter, *Astrophys. J.*, 186, 1097–1106.

Flasar, F. M., et al. (2004), Exploring the Saturn system in the thermal infrared: The composite infrared spectrometer, *Space Sci. Rev.*, 115, 169–297.

Flasar, F. M., et al. (2005), Temperatures, winds, and composition in the Saturnian system, *Science*, 307, 1247–1251.

Fletcher, L. N., R. K. Achterberg, T. Greathouse, G. Orton, B. Conrath, A. A. Simon-Miller, S. Guerlet, N. Teanby, P. Irwin, and F. M. Flasar (2010), Seasonal change on Saturn from Cassini/CIRS 2004–2009, *Icarus*, 208, 337–352.

Gautier, D., and R. Courtn (1979), Atmospheric thermal structures of the giant planets, *Icarus*, 39, 28–45.

Goody, R. M., and Y. L. Yung (1989), *Atmospheric Radiation: Theoretical Basis*, 2nd ed., Oxford Univ. Press, Oxford, New York.

Hanel, R., D. Crosby, L. Herath, D. Vanous, D. Collins, H. Creswick, C. Harris, and M. Rhodes (1980), Infrared spectrometer for Voyager, *Appl. Opt.*, 19, 1391–1400.

Hanel, R. A., B. J. Conrath, V. G. Kunde, J. C. Pearl, and J. A. Pirraglia (1983), Albedo, internal heat-flux, and energy-balance of Saturn, *Icarus*, 53, 262–285.

Hanel, R. A., B. J. Conrath, D. E. Jennings, and R. E. Samuelson (2003), *Exploration of the Solar System by Infrared Remote Sensing*, Cambridge Univ. Press, New York.

Hass, M. R., E. E. Erickson, D. D. Mckibbin, D. Goorvitch, and L. J. Caroff (1982), Far-infrared spectrophotometry of Saturn and its rings, *Icarus*, 51, 476–490.

Heimpel, M., and J. Aurnou (2007), Turbulent convection in rapidly rotating spherical shells: A model for equatorial and high latitude jets on Jupiter and Saturn, *Icarus*, 187, 540–557.

Ingersoll, A. P. (1990), Atmospheric dynamics of the outer planets, *Science*, 248, 308–315.

Ingersoll, A. P., G. Munch, G. Neugebauer, D. J. Dineer, G. S. Orton, B. Schupler, M. Schroeder, S. C. Chase, R. D. Ruiz, and L. M. Trafton (1975), Pioneer 11 infrared radiometer experiment—Global heat balance of Jupiter, *Science*, 188, 472–473.

Ingersoll, A. P., G. S. Orton, G. Munch, G. Neugebauer, and S. C. Chase (1980), Pioneer Saturn infrared radiometer—Preliminary results, *Science*, 207, 439–443.

Kunde, V. G., et al. (1996), Cassini infrared Fourier spectroscopic investigation, in *Cassini/Huygens: A Mission to the Saturnian Systems*, *Proc. SPIE*, vol. 2803, edited by L. Horn, pp. 162–177.

Lean, J. L., and D. H. Rind (2009), How will Earth's surface temperature change in future decades?, *Geophys. Res. Lett.*, 36, L15708, doi:10.1029/2009GL038932.

Li, L., A. P. Ingersoll, and X. L. Huang (2006), Interaction of moist convection with zonal jets on Jupiter and Saturn, *Icarus*, 180, 113–123.

Li, L., P. J. Gierasch, R. K. Achterberg, B. J. Conrath, F. M. Flasar, A. R. Vasavada, A. P. Ingersoll, D. Banfield, A. A. Simon-Miller, and L. N. Fletcher (2008), Strong jet and a new thermal wave in Saturn's equatorial

stratosphere, *Geophys. Res. Lett.*, 35, L23208, doi:10.1029/2008GL035515.

Melnick, G., R. W. Russell, T. R. Gossnell, and M. Harwit (1983), Spectrophotometry of Saturn and its rings from 60 to 180 Mirons, *Icarus*, 53, 310–318.

Nixon, C. A., D. E. Jennings, J. M. Flaud, B. Bezard, N. A. Teanby, P. G. J. Irwin, T. M. Ansty, A. Coustenis, S. Vinatier, and F. M. Flasar (2009), Titan's prolific propane: The Cassini CIRS perspective, *Planet. Space Sci.*, 57, 1573–1585.

Nolt, I. G., J. V. Radostitz, R. J. Donnelly, R. E. Murphy, and H. C. Ford (1977), Thermal emission of Saturn's rings and disk at 34 μm, *Nature*, 248, 659–660.

Orton, G. S., and A. P. Ingersoll (1980), Saturn's atmospheric-temperature structure and heat-budget, *J. Geophys. Res.*, 85(A11), 5871–5881, doi:10.1029/JA085iA11p05871.

Perez-Hoyos, S., and A. Sanchez-Lavega (2006), Solar flux in Saturn's atmosphere: Penetration and heating rates in the aerosol and cloud laggers, *Icarus*, 180, 368–278.

Perez-Hoyos, S., A. Sanchez-Lavega, R. G. French, and J. F. Rojas (2005), Saturn's cloud structure and temporal evolution from ten years of Hubble Space Telescope images (1994–2003), *Icarus*, 176, 155–174.

Read, P. L., B. J. Conrath, L. N. Fletcher, P. J. Gierasch, A. A. Simon-Miller, and L. C. Zuchowski (2009), Mapping potential vorticity dynamics on Saturn: Zonal mean circulation from Cassini and Voyager data, *Planet. Space Sci.*, 57, 1682–1698.

Salpeter, E. (1973), On convection and gravitational layering in Jupiter and stars of low mass, *Astrophys. J.*, 181, L83–L86.

Schneider, T., and J. J. Liu (2008), Formation of jets and equatorial super-rotation on Jupiter, *J. Atmos. Sci.*, 66, 579–601.

Showman, A. P. (2008), Numerical simulations of forced shallow-water turbulence: Effects of moist convection on the large-scale circulation of Jupiter and Saturn, *J. Atmos. Sci.*, 64, 3132–3157.

Smoluchowski, R. (1976), Internal structure and energy emission of Jupiter, *Nature*, 215, 691–695.

Stevenson, D. J., and E. E. Salpeter (1976), The dynamics and helium distributions in hydrogen-helium planets, *Astrophys. J. Suppl.*, 35, 239–261.

Ward, D. B. (1977), Far-infrared spectral observations of Saturn and its rings, *Icarus*, 32, 437–442.

Wright, E. L. (1976), Recalibration of the far-infrared brightness temperatures of the planets, *Astrophys. J.*, 210, 250–253.

R. K. Achterberg and C. A. Nixon, Department of Astronomy, University of Maryland, College Park, MD 20742, USA.

K. H. Baines, G. S. Orton, A. R. Vasavada, and R. A. West, Jet Propulsion Laboratory, California Institute of Technology, Pasadena, CA 91109, USA.

D. Banfield, B. J. Conrath, and P. J. Gierasch, Department of Astronomy, Cornell University, Ithaca, NY 14853, USA.

G. L. Bjoraker, F. M. Flasar, and A. A. Simon-Miller, NASA Goddard Space Flight Center, Greenbelt, MD 20771, USA.

A. D. Del Genio, NASA Goddard Institute for Space Studies, New York, NY 10025, USA.

L. N. Fletcher, P. G. J. Irwin, and P. L. Read, Atmospheric, Oceanic and Planetary Physics, University of Oxford, Parks Road, Oxford OX1 3PU, UK.

A. P. Ingersoll, Division of Geological and Planetary Sciences, California Institute of Technology, Pasadena, CA 91125, USA.

L. Li, Department of Earth and Atmospheric Sciences, University of Houston, Houston, TX 77204, USA. (lli7@mail.uh.edu)

A. A. Mamoutkine, Science Systems and Applications Inc., Lanham, MD 20706, USA.

C. C. Porco, CICLOPS/Space Science Institute, Boulder, CO 80302, USA.

M. E. Segura, QSS Group, Inc., Lanham, MD 20706, USA.